PNAS RESEARCH ARTICLE | EARTH, ATMOSPHERIC, AND PLANETARY SCIENCES OPEN ACCESS

Fault roughness controls injection-induced seismicity

Lei Wang[a,1], Grzegorz Kwiatek[a], François Renard[b,c,d], Simon Guérin-Marthe[a,e], Erik Rybacki[a], Marco Bohnhoff[a,f], Michael Naumann[a], and Georg Dresen[a,g]

Edited by Peter Kelemen, Lamont-Doherty Earth Observatory, Palisades, NY; received June 20, 2023; accepted December 4, 2023

Surface roughness ubiquitously prevails in natural faults across various length scales. Despite extensive studies highlighting the important role of fault geometry in the dynamics of tectonic earthquakes, whether and how fault roughness affects fluid-induced seismicity remains elusive. Here, we investigate the effects of fault geometry and stress heterogeneity on fluid-induced fault slip and associated seismicity characteristics using laboratory experiments and numerical modeling. We perform fluid injection experiments on quartz-rich sandstone samples containing either a smooth or a rough fault. We find that geometrical roughness slows down injection-induced fault slip and reduces macroscopic slip velocities and fault slip-weakening rates. Stress heterogeneity and roughness control hypocenter distribution, frequency–magnitude characteristics, and source mechanisms of injection-induced acoustic emissions (AEs) (analogous to natural seismicity). In contrast to smooth faults where injection-induced AEs are uniformly distributed, slip on rough faults produces spatially localized AEs with pronounced non-double-couple source mechanisms. We demonstrate that these clustered AEs occur around highly stressed asperities where induced local slip rates are higher, accompanied by lower Gutenberg–Richter *b*-values. Our findings suggest that real-time monitoring of induced microseismicity during fluid injection may allow identifying progressive localization of seismic activity and improve forecasting of runaway events.

laboratory earthquakes | fluid-induced seismicity | fault roughness | stress heterogeneity | aseismic slip

Significance

Fluid-induced earthquakes associated with industrial activities, such as wastewater disposal, geothermal energy production, and CO_2 storage, have received increasing scientific concerns. Natural faults that host earthquakes typically display nonplanar structures. This study provides straightforward information on how fault structure and heterogeneity control injection-induced fault slip and associated seismicity characteristics using well-designed fluid injection experiments on laboratory faults and relevant numerical modeling. The results indicate that geometrical roughness slows down injection-induced fault slip and affects hypocenter distribution, frequency–magnitude characteristics, and source mechanisms of induced seismicity. We highlight the key roles that fault roughness and stress heterogeneity play in modulating a transition from aseismic to seismic slip when subjected to increased fluid pressure, leading to large induced events localized around highly stressed asperities.

Geometrical roughness, the deviation from a planar surface, characterizes natural faults over a wide range of length scales (1–5), exhibiting a consistent self-affine scaling law. A plethora of studies have demonstrated that the presence of geometric asperities on faults results in significantly heterogeneous stress distributions (6–11). Fault roughness and heterogeneous local stresses affect nucleation, propagation, and arrest of shear ruptures (10, 12, 13), foreshock, mainshock, and aftershock sequences (14, 15), and coseismic slip distribution and locations of earthquake hypocenters (16, 17). Likewise, ground motion, radiation pattern and source parameters of seismic events (17–19), and the distribution of off-fault damage zones (8, 17, 20) are linked to fault structures. Laboratory friction experiments highlight the important role of fault roughness in controlling rupture nucleation and slip instability (21–27). When compared to smooth faults, rough faults display longer nucleation time and larger nucleation length but lower macroscopic slip velocities and a wider range of rupture speeds (21, 25, 26, 28). Moreover, rate-and-state friction parameters, experimentally derived from laboratory experiments performed on samples with varying fault roughness, showed different and opposing trends with roughness (29–32). In addition to the rich mechanical behavior, spatial distribution and statistical characteristics of acoustic emission (AE) events associated with failure of microscopic asperities are closely linked to fault surface morphology (23, 24, 33).

Fluid injection into the subsurface may cause a preexisting fault to slip seismically and induce seismic events (anthropogenic earthquakes), which have been documented worldwide in enhanced geothermal system, waste-water injection, and geologic sequestration of carbon dioxide (34, 35). Fault reactivation associated with fluid injection may occur as a result of a reduction of effective normal stress unclamping the fault, poroelastic stress changes, and/or stress transfer through aseismic slip (34–37). Extensive geophysical surveys document the occurrence of induced earthquakes being affected by fluid pressure, injection rate, and fluid volume injected (38–41). Theoretical models (42–44) and laboratory experiments (45–48) also suggest causal relations between stimulation parameters and seismic activity. In addition to fluid injection parameters, complex injection-induced slip behavior may emerge depending on background stress states (49–51), pressure-dependent frictional properties (36), and the interplay between permeability change and fault slip (37, 52). While the effects of surface roughness on tectonic earthquakes have been extensively explored, the role of fault structure and heterogeneity on induced seismicity remains

Author contributions: L.W. and G.D. designed research; L.W. performed research; L.W., G.K., and M.B. contributed new reagents/analytic tools; L.W., G.K., F.R., S.G.-M., E.R., M.B., M.N., and G.D. analyzed data; and L.W. and G.D. wrote the paper.

The authors declare no competing interest.

This article is a PNAS Direct Submission.

[1]To whom correspondence may be addressed. Email: wanglei@gfz-potsdam.de.

This article contains supporting information online at https://www.pnas.org/lookup/suppl/doi:10.1073/pnas.2310039121/-/DCSupplemental.

Published January 12, 2024.

elusive. Several numerical simulations of injection-induced ruptures on rough faults suggest that stress heterogeneity arising from fault roughness primarily controls rupture size and seismic moment release, in addition to fluid pressure and injected volume (53, 54). A limited number of experiments indicate that surface roughness of laboratory faults in granite samples alters fault hydraulic properties, giving rise to varying fluid pressure distributions and slip responses (55–57). The spatiotemporal distribution of fluid pressure in these experiments suggested that pressure heterogeneity and stress heterogeneity were highly coupled, complicating the interpretation of observed fault slip.

In this work, we experimentally investigate the effect of fault roughness and stress heterogeneity on injection-induced fault slip. We disentangle the effects of stress heterogeneity and pressure heterogeneity using highly permeable quartz-rich sandstone samples as testing materials so that fluid pressure rapidly equilibrates throughout the entire sample volume. To explore the effect of geometrical roughness, we prepare saw-cut and polished laboratory faults and rough shear-fractured samples for fluid injection experiments. Results show that complex fault geometry slows down injection-induced fault slip and exerts a strong control on spatial distribution, frequency–magnitude characteristics, and source mechanisms of injection-induced AE events. For further analysis of the observed effects of fault and stress heterogeneity, we compare the experimental data to numerical modeling results of fault slip on smooth and rough faults.

Results

We have loaded cylindrical samples containing an inclined fault interface with varying surface roughness (saw-cut smooth surface vs. fractured rough surface) in a triaxial compression apparatus to a critical stress state and subsequently activated fault slip using defined fluid injection protocols (Fig. 1*A*, *Materials and Methods*). To study the effect of geometrical roughness on induced fault slip, we have produced a series of injection-induced slip events on three samples, one containing a smooth fault and two samples cut by rough faults (rough fault #1 and rough fault #2, respectively) at fixed boundary conditions. In striking contrast to the smooth saw-cut fault with a spatially uniform and very flat surface topography (Fig. 1*B*), the two fractured faults display significant surface roughness with maximum height difference up to 7 mm (Fig. 1*C*

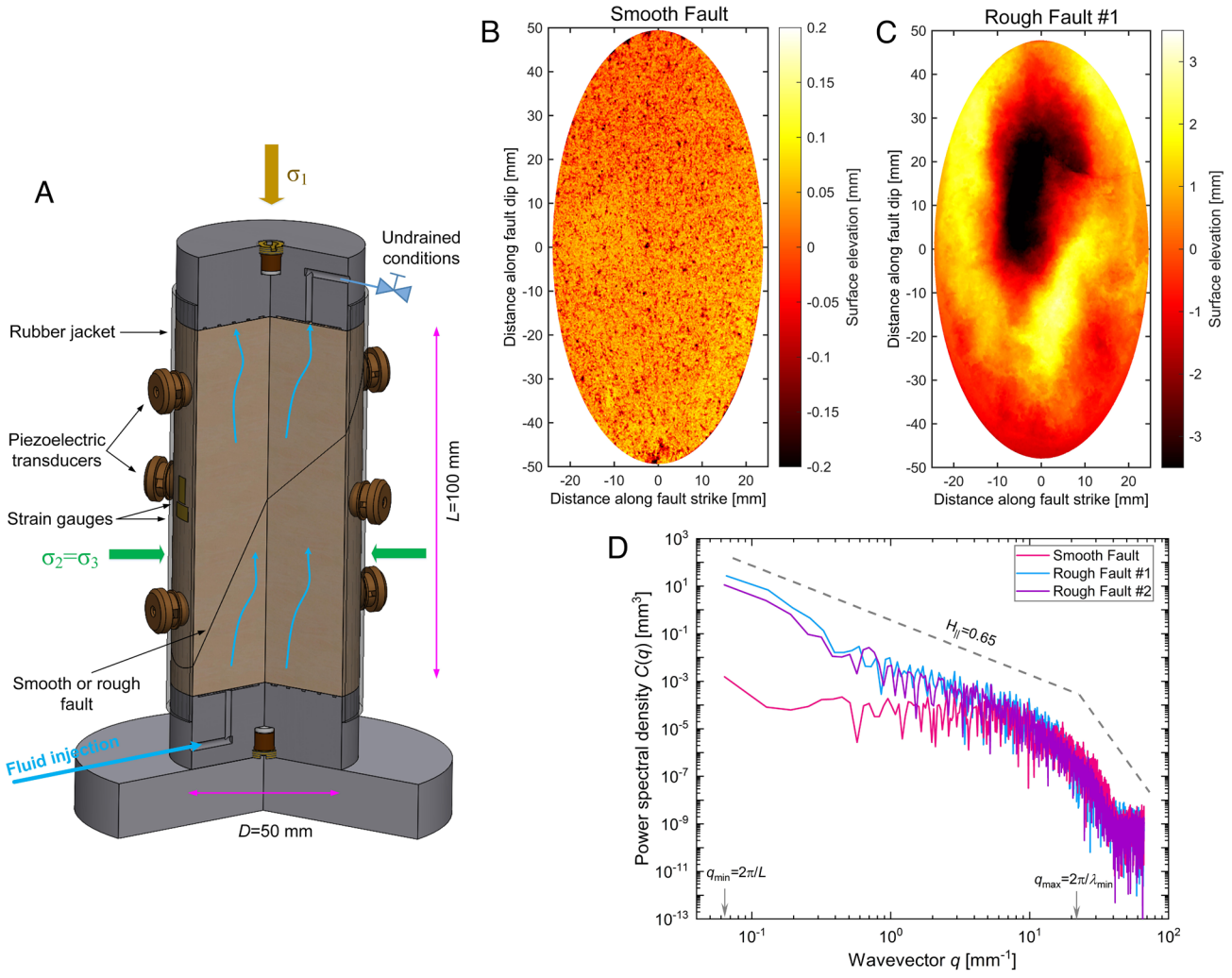

Fig. 1. Experimental setup and prepared laboratory faults with varying surface roughness. (*A*) Fluid injection experiments performed on cylindrical samples (50 × 100 mm) of a permeable quartz-rich sandstone containing an inclined (ϕ = 30° relative to the loading axis) smooth or rough fault subjected to triaxial compression. The samples are mounted with an array of strain gauges and piezoelectric transducers. (*B* and *C*) Surface elevation of the lower rock block for the smooth (saw-cut) and rough (shear-fractured) faults, respectively. (*D*) Power spectral density (PSD) of surface profiles along fault slip direction for smooth and rough faults. q_{min} and q_{max} mean the minimum and maximum wavevector while L and λ_{min} indicate fault length and the minimum wavelength, respectively. Two rough laboratory faults display a broad-band (from quartz grain size λ_{min} ≈ 0.3 mm to fault length L = 100 mm) self-affine roughness with a Hurst exponent $H_{\parallel}$ of 0.65. In contrast, the PSD of the saw-cut fault across the similar wavelength range is almost flat and does not follow a power law.

and *SI Appendix*, Fig. S2). Using fast Fourier transform, the power spectral density (PSD) of the elevation profiles parallel and perpendicular to fault dip reveals a broad-band (from quartz grain size to fault length) self-affine roughness with a Hurst exponent of about 0.65 (Fig. 1*D* and *SI Appendix*, Fig. S3). In contrast, the PSD of the smooth saw-cut fault across the similar wavelength range is almost flat and does not follow a power law.

Injection-Induced Slip Behavior on Experimental Faults with Varying Roughness. We report two representative experiments on samples with substantially different fault roughness where fluid pressure along a critically stressed fault is increased stepwise. The cylindrical samples containing a saw-cut or rough fault interface inclined at $\phi = 30°$ relative to the axis are loaded axially at a constant confining pressure $\sigma_3 = 35$ MPa and fluid pressure $p = 5$ MPa, leading to a progressive increase in resolved shear stress with slip up to a peak shear strength τ_{ss} (stage 1 in Fig. 2 *A* and *C*). When approaching τ_{ss}, shear stress is almost constant while the fault slip rate accelerates to a steady-state value, roughly equal to the imposed load point velocity of the ram (*SI Appendix*, Fig. S5*A*). Shear stress data show small hardening for both smooth and rough faults (Fig. 2 *A* and *C*), and the values of τ_{ss} and corresponding steady-state friction coefficients scale with the rms roughness of fault surface (*SI Appendix*, Fig. S5*D*). This result indicates that

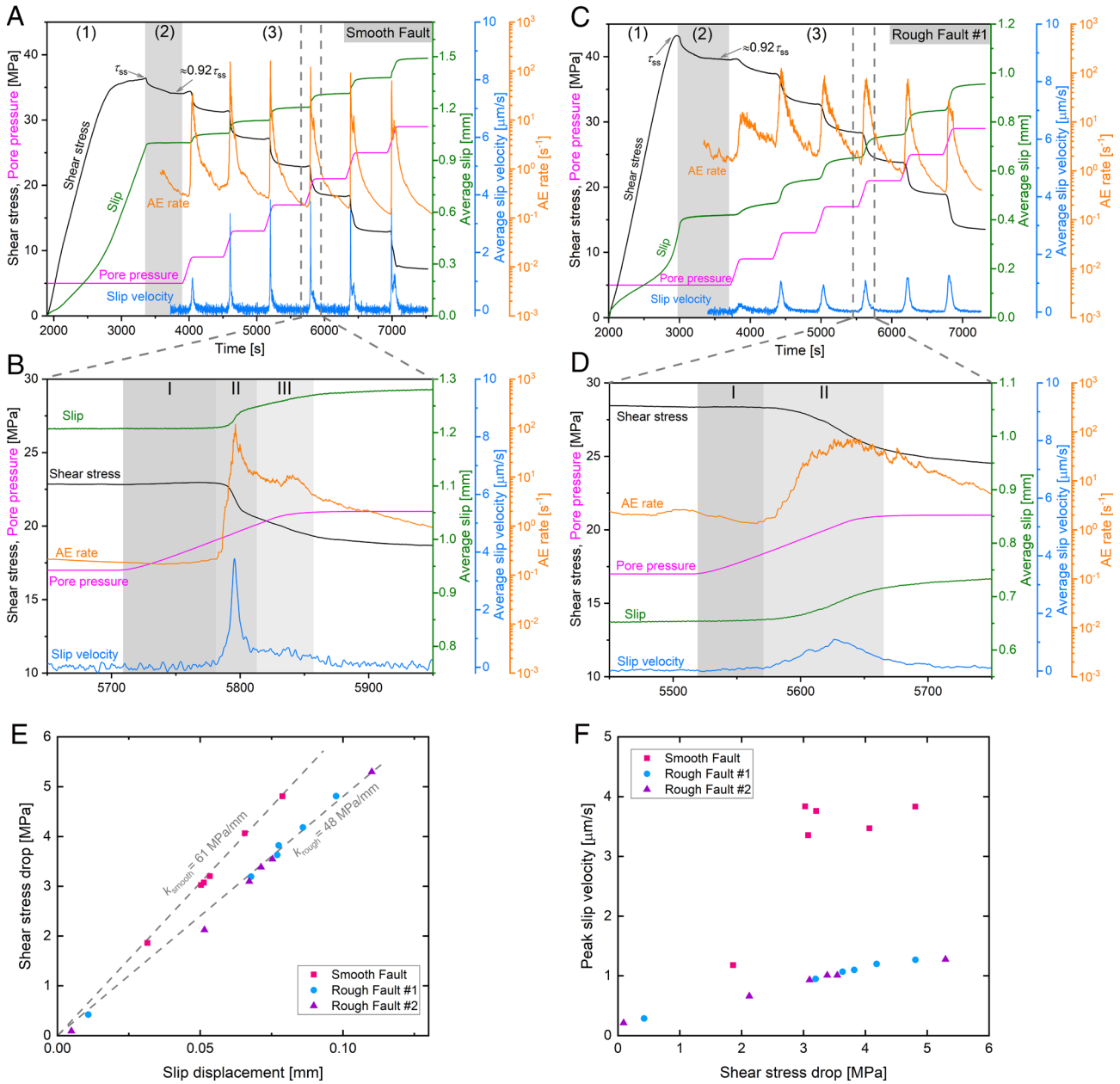

Fig. 2. Mechanical behavior of injection-induced fault slip on smooth and rough faults. (*A* and *C*) Temporal evolution of shear stress, fluid pressure, AE rate, and average fault slip and slip rate observed on the smooth fault and rough fault #1, respectively. The experimental procedure is divided into three stages, as indicated by labels 1, 2 and 3, respectively. After the shear strength (τ_{ss}) is achieved in stage 1, shear stress is then reduced to about 0.92 τ_{ss} in stage 2, followed by a six-stage fluid injection scheme in stage 3. (*B* and *D*) Zoomed details on injection-induced fault slip, AE rate, etc., during the fourth fluid injection stage for smooth and rough faults, respectively. In response to fluid pressurization, the smooth fault undergoes three different phases with time, as indicated by shaded areas with labels I, II, and III. In contrast, two phases are observed on the rough fault. (*E*) Compiled slip displacements and associated shear stress drops during injection-induced slip events in smooth and rough faults. The linear regressions to the data, as shown by the gray dashed lines, correspond to slip-weakening rates (unloading stiffnesses) of smooth and rough faults. (*F*) Compiled peak slip velocities of induced slip events during six fluid injection stages as a function of stress drops in the smooth and rough faults.

geometrical roughness introduces an additional shear resistance to continuous slip, consistent with results from theoretical and numerical models (8, 10, 13). In stage 2, we adjust the shear stress to about 0.92 τ_{ss} for the saw-cut fault and rough fault #1 (Fig. 2 *A* and *C*) and to about 0.86 τ_{ss} for rough fault #2 (*SI Appendix*, Fig. S4*A*), respectively. Initial effective normal and shear stresses are 50.1 MPa and 34.0 MPa for the saw-cut fault, 53.0 MPa and 39.5 MPa for rough fault #1, and 49.6 MPa and 33.5 MPa for rough fault #2, respectively. We then keep the axial piston position fixed to ensure a zero-displacement condition on the two extremities of the sample and then start fluid injection. We follow a six-stage fluid injection scheme where fluid pressure is increased in a stepwise manner from 5 MPa to 29 MPa with a pressurization rate of 2 MPa/min. During each fluid injection stage, fluid pressure increment of 4 MPa is achieved within 2 min, followed by a plateau phase lasting for 8 min.

Due to the high sample permeability (10^{-12} m^2), fluid pressure rapidly equilibrates on the order of milliseconds within the whole sample volume (46, 58). With the onset of fluid injection, slip along smooth and rough faults initiates with a delay that progressively decreases with subsequent injection cycles (stage 3 in Fig. 2 *A* and *C* and Movies S1 and S2). The smooth fault displays episodic slow stick-slip events during injection with a peak slip velocity increasing to about 3.8 μm/s, accompanied by increasing stress drops and rapid AE bursts with a peak rate up to 150 events per second (Fig. 2*A*). In stark contrast, at similar conditions and fluid pressurization rates induced slip events along the rough faults reach lower peak slip velocities of about 1.0 μm/s (Fig. 2*C*). Here, peak AE rates and subsequent decay rates with time are lower for rough surfaces, but stress drops increase with consecutive slip events. Our experiments highlight that fault roughness promotes the stability of injection-induced fault slip.

The strong dependence of the evolving injection-induced fault slip rate on geometrical roughness is shown in detail in the zoomed fourth fluid injection stage (Fig. 2 *B* and *D*). After fluid pressurization is started, the smooth fault first remains locked for about 73 s (phase I in Fig. 2*B*). Then, fault slip initiates and rapidly accelerates to peak slip rate, which then decreases to a residual value of about 0.6 μm/s in about 28 s (phase II in Fig. 2*B*), followed by a long-lasting relaxation phase with minor oscillations in slip velocity and in AE rate upon the termination of fluid injection (phase III in Fig. 2*B*). The evolving slip rate is closely correlated with the AE rate.

Compared to the smooth fault, the rough faults first undergo a shorter delay of 40 to 50 s after fluid injection starts (phase I in Fig. 2*D* and *SI Appendix*, Fig. S4*B*). Peak slip velocity and acceleration are smaller with a prolonged relaxation phase (phase II in Fig. 2*D* and *SI Appendix*, Fig. S4*B*). Despite the minor difference in initial stress levels between the two rough faults, the results from these two samples are similar.

To compare the difference in slip dynamics between smooth and rough faults, we compile slip displacement, peak slip velocity, and associated stress drop during injection-induced slip events. The slope of average shear stress drops with average slip displacements associated with slip events determines the average fault slip-weakening rate (unloading stiffness) (Fig. 2*E*), that is K_{smooth} = 61 MPa/mm for the smooth fault and K_{rough} = 48 MPa/mm for the rough faults. Peak slip velocities of injection-induced slip events increase with stress drop for both smooth and rough faults but are very different depending on fault roughness (Fig. 2*F*).

Characteristics of Injection-Induced Acoustic Emissions. A set of 16 piezoelectric transducers surrounding the sample allow us to monitor and locate AE events associated with injection-induced fault slip (*SI Appendix*, section 3). Spatial characteristics and statistical attributes of AEs provide fundamental insights into the role of varying surface roughness on fluid-induced seismicity.

We have located a total number of 3,983, 7,627, and 6,390 AEs during fluid injection for smooth fault, rough fault #1, and rough fault #2, respectively. The three-dimensional spatial distribution of AE hypocenters varies significantly with surface roughness. For the smooth saw-cut fault, injection-induced slip events generate an AE hypocenter distribution that is forming a narrow band surrounding the fault plane with a half-width normal to the fault surface of about 2 mm (i.e., similar to location accuracy of AE hypocenters) (*SI Appendix*, Fig. S6). For the rough faults, the AEs form a zone of about 10 mm width normal to the fault due to fault topography and wall rock damage (*SI Appendix*, Fig. S7). In two-dimensional map view with all AE hypocenters projected onto the fault, AEs are homogeneously distributed across the smooth fault (Fig. 3*A*). In contrast, fluid injection into the rough faults results in AE events forming distinct local clusters (Fig. 3*D*). Spatial distribution of clustered AEs on rough faults is characterized by a fractal dimension *D* of about 1.4 compared to a more planar AE distribution with a *D*-value ≈1.8 on the smooth fault (*SI Appendix*, section 5 and Fig. S8). The intense clustering of induced AEs is closely correlated with the local gradient of surface topography along slip direction (Fig. 3*D*), mapping the spatial distribution of highly stressed asperities on the rough fault. In general, a larger positive gradient of surface topography corresponds to the local shear and normal stress concentrations at restraining bends (12, 16, 17), promoting the occurrence of large-magnitude events (59, 60).

The frequency–magnitude distribution of induced AEs and resulting *b*-value have been impacted by fault surface topography (see *SI Appendix*, section 6 for *b*-value calculation). We have registered more total AE events with larger AE magnitudes on the two rough faults and the calculated *b*-values for AEs are slightly lower compared to the smooth fault (*SI Appendix*, Fig. S9). Changes in *b*-values are assumed to reflect local stress states and geometry of the fracture network (23, 24, 61). For the rough faults, the presence of highly stressed asperities and substantial off-fault damage may contribute to higher AE productivity and a larger fraction of high-magnitude AE events. To identify fault heterogeneity, we additionally provide the spatial distribution of AE seismic moment release (*SI Appendix*, section 7) and associated *b*-value maps (Fig. 3 *B*, *C*, *E*, and *F*). Substantial seismic moment release of AEs is produced in the vicinity of high-stress patches during induced slip events, accompanied by lower *b*-values (Fig. 3*F* and *SI Appendix*, Fig. S10). This result suggests that the spatial variation of *b*-values is closely coupled to local stress conditions over the fault surface and may assist in mapping seismogenic fault segments for induced seismicity and natural earthquakes (62).

Fault roughness also affects off-fault damage, as observed by postmortem microstructures (*SI Appendix*, section 10). For the initial smooth fault surface, cumulative slip results in a thin layer (half-width < 0.5 mm, about 1 to 2 original grain diameters) of fine-grained gouge that is relatively uniform across the principal slip surface (*SI Appendix*, Fig. S11 *A* and *B*). Significant fragmentation and comminution of quartz grains adjacent to the fault surface result in high-frequency wave radiation, as evidenced by a homogeneous distribution of AE activity recorded across the smooth fault. Shear deformation is distributed and mainly accommodated by grain fragmentation and shear-induced rotation. In contrast, off-fault damage surrounding the rough fault surface consists of gouge layers, which are thicker (half-width ≈ 1 mm) compared to the smooth fault but varies along the fault (*SI Appendix*, Fig. S11*C*). Intense cataclastic deformation prevails

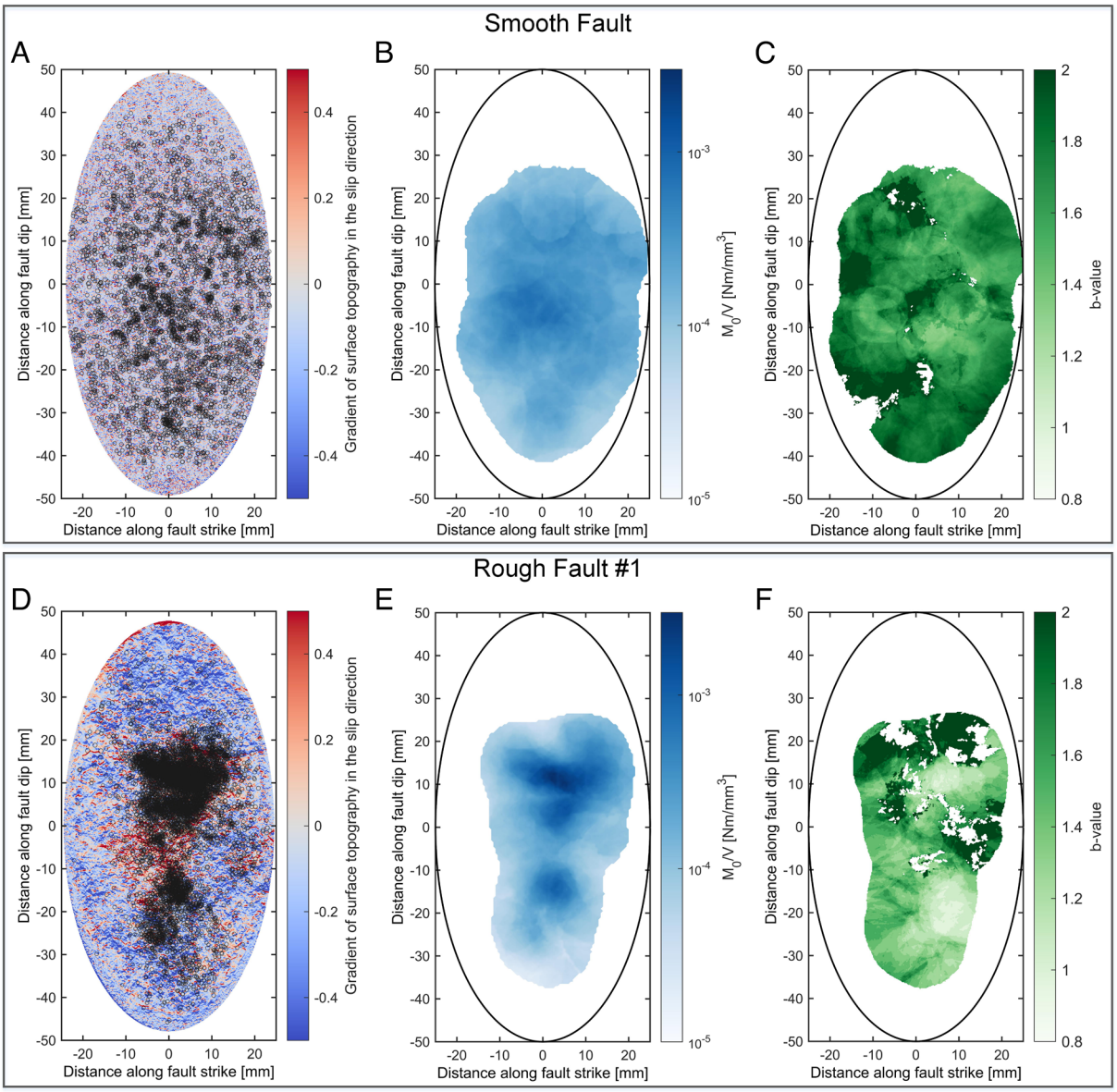

Fig. 3. Characteristics of injection-induced AEs at the smooth and rough faults. (*A* and *D*) Map views showing all induced AEs from experiments performed on smooth and rough faults, respectively, with their hypocenters projected onto the fault plane. AE events are displayed using black open circles with sizes proportional to AE magnitudes. The fault plane of the lower rock block is color-coded by the local gradient of surface topography along fault down-dip (i.e., slip direction of the upper rock block relative to its counterpart). (*B* and *E*) Maps of seismic moment release per elementary volume (M_0/V) using full AE catalogs for the smooth and rough faults, respectively. (*C* and *F*) Spatial variations of Gutenberg–Richter *b*-value for all induced AEs of the smooth and rough faults, respectively. Note that *b*-values are only shown here for bins containing sufficient AE events (>150 AEs) and the goodness of fit for the Gutenberg–Richter law larger than 90%.

at restraining bends, also displaying a dense distribution of AE events (Fig. 3*D*). The formation of multiple discrete shear planes accommodating local slips is more pronounced for rough faults (*SI Appendix,* Fig. S11*D*). The observed off-fault crack damage corresponds with the AE density distribution decreasing with distance from the fault surface (*SI Appendix,* Fig. S12). Progressive clustering of AEs induced by fluid injection is characterized by a peak in AE density distribution centered around the fault interface, and a rapid decay toward the adjacent wall-rock, consistent with previous laboratory studies of fracture propagation and stick-slip (23) and the documented natural seismicity across strike-slip faults in California (63).

To evaluate the AE source kinematics, we employ the average polarity of first P-wave amplitudes (64) and full moment tensor (FMT) inversion method (65) (*SI Appendix*, section 8). Based on either the average polarity (64) or the FMT decomposition results (66, 67), AE source mechanism can be categorized into a shear, compaction or tensile type. The average polarity analysis shows a good agreement with the FMT solution results, indicating domination of shear- and compaction-type events (Fig. 4 *A* and *B* and *SI Appendix,* Fig. S13). For the smooth fault, the source mechanisms of induced AEs are dominated by shear-type (double-couple) events, accounting for 65 to 75% of all AEs compared to about 30 to 45% for the rough faults (Fig. 4*C*). In rough faults, we find a relative increase of non-double-couple source types with respect to the shear events, confirming that fault roughness affects kinematics of injection-induced seismicity, similar to what has been reported in an earlier study without fluid injection (68).

Numerical Simulation of Injection-Induced Fault Slip and Slip Rate. To further investigate roughness effects on injection-induced slip and slip rate distributions, we employ a numerical model.

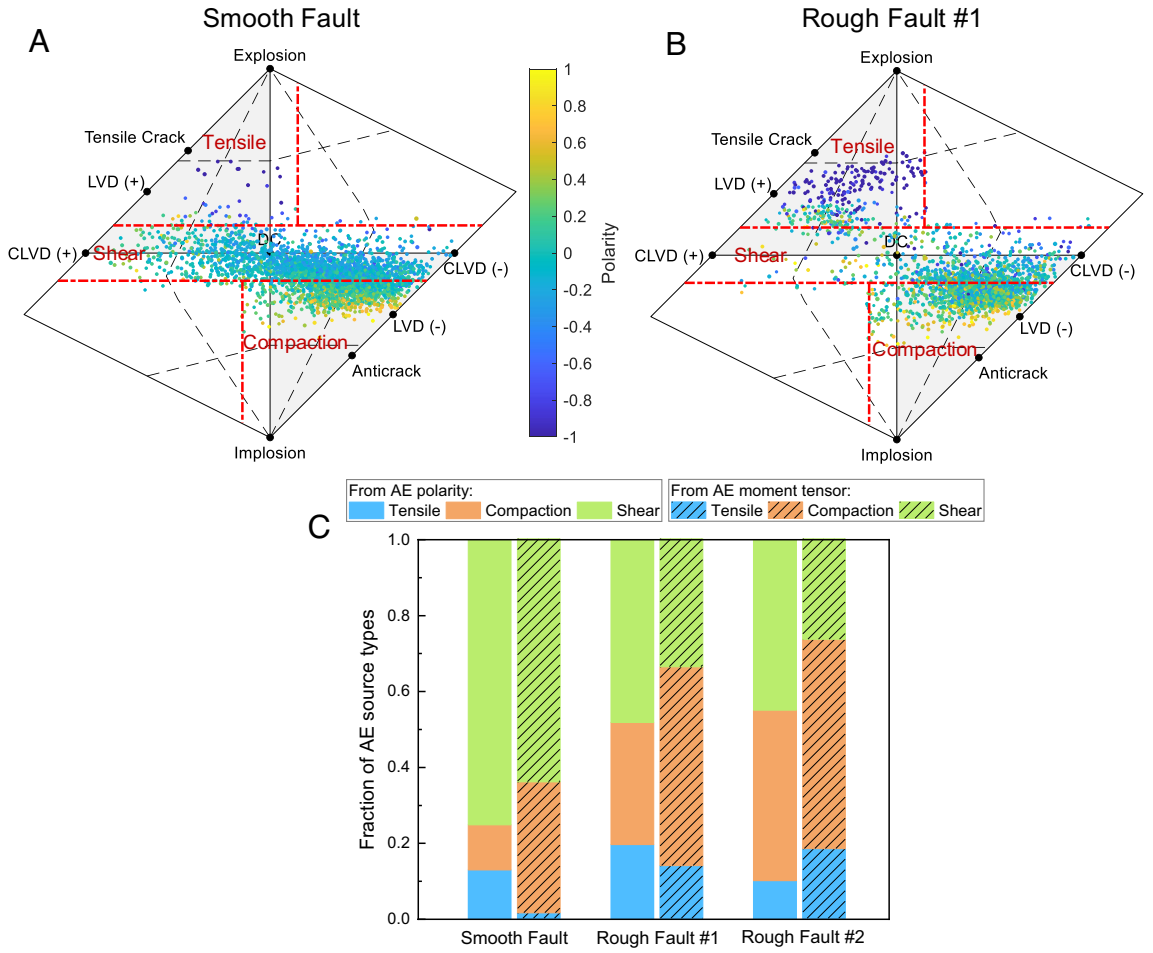

Fig. 4. Source mechanisms of all induced AEs derived from the average polarity method and full moment tensor inversion method. (*A* and *B*) Hudson equal-area diagram showing the AE source mechanisms for the smooth and rough fault #1, respectively. In the Hudson diagram, DC denotes double couple, CLVD denotes compensated linear vector dipole, and LVD is linear vector dipole (see ref. 66 for details). The volumetric and nonvolumetric (shear) source kinematics are separated by the dashed red lines (67). The AE source kinematics are also color-coded by average polarity coefficient with values of 1.0 and −1.0 corresponding to pure compaction-type and tensile-type events, respectively. (*C*) AE source type fractions for all induced AE events on smooth and rough faults. AE source mechanisms may be separated into tensile, shear, and compaction types, based on either the average polarity or the full moment tensor solution.

We couple a one-dimensional Burridge–Knopoff model with a heterogeneously loaded fault interface and the rate-and-state friction law with a fluid pressure diffusion process (see *Materials and Methods* for model formulation). We use a total number of equally spaced 100 slider blocks with a grid spacing of 1 mm (i.e., the block size) to simulate injection-induced slip along the 100 mm-long laboratory faults. Considering the homogeneous and isotropic rock materials used in the experiments, we assume spatially uniform frictional properties but account for stress heterogeneity arising from fault roughness. We first estimate the two-dimensional static stress distribution produced by frictional slip along a wavy fault in elastic media using an analytical model (7). For rough fault #1, high normal, shear, and differential stresses generally concentrate around restraining bends (*SI Appendix*, section 11 and Fig. S15), in agreement with the observed abundant AEs. In contrast to highly homogeneous stresses prevailing along the smooth fault, the initially heterogeneous normal and shear stresses along rough fault #1 before fluid injection are then imported into the model for simulating subsequent injection-induced fault slip behavior (*SI Appendix*, Fig. S16). We employ the experimentally observed slip onsets and the magnitudes of measured average slip velocities induced by fluid injection to benchmark our numerical models.

We use the experimentally measured rate-and-state frictional parameters of $(a-b) \approx -10^{-3}$ and $d \approx 5$ μm for the smooth (saw-cut) fault in Bentheim sandstone (*SI Appendix*, section 11). Modeled slip onsets, peak slip velocities, and subsequent small oscillations in slip rates along smooth faults are in good agreement with the experimental data (Fig. 5*A*). Homogeneous normal and shear stresses and fluid pressure increments distributed across the smooth fault result in spatially uniform slip and slip rates, as documented by the distribution of located AEs (Fig. 5*B*).

Assuming that the characteristic slip distance d in the rate-and-state friction formulation scales with surface roughness and shear band thickness (31, 32), we increase d from 5 μm for the smooth fault to 10 μm for the rough fault while the other friction constitutive parameters (a and b) remain unchanged (*SI Appendix*, section 11). We obtain a good agreement between modeled and observed average slip velocities measured on the rough fault. In contrast to the smooth fault, the induced slip and slip rate distributions on the rough fault show high spatial variability (Fig. 5 *C* and *D*). Although our numerical model assumes a chain of undeformed but interconnected blocks and does not account for the strain field, the observed spatial variability in slip and slip rate implicitly reflects a heterogeneous strain distribution, consistent with the differently evolving strain fields monitored by local strain gauges mounted close to the fault interface (*SI Appendix*, Fig. S18). Ruptures initiate almost simultaneously at two fault segments favorably oriented for slip (i.e., the low-stress regions with large

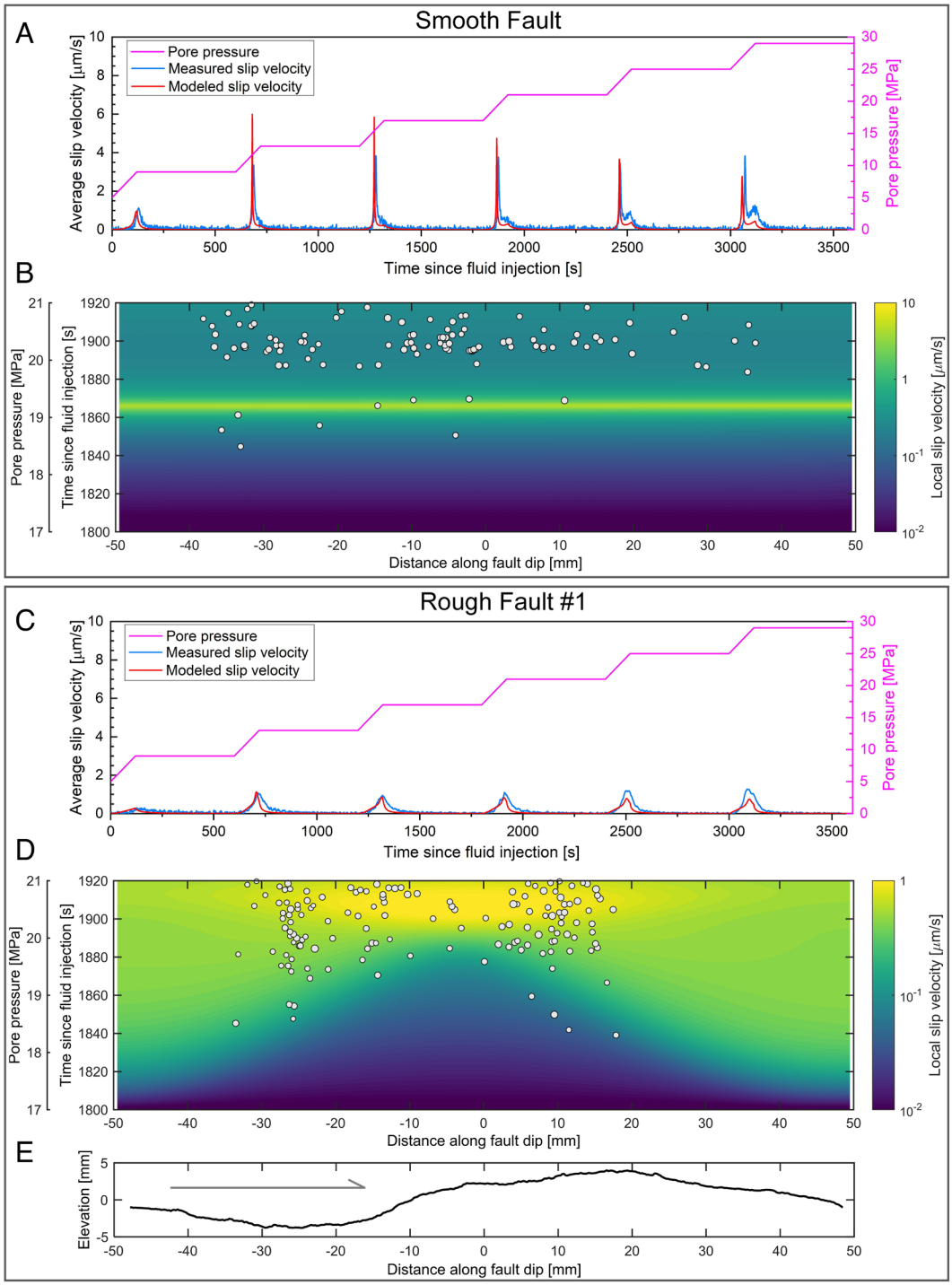

Fig. 5. Numerical simulations showing temporal evolution of injection-induced average and local fault slip velocities along fault dip for the smooth and rough faults. (*A* and *C*) Comparisons of evolving average slip velocities from experimental measurements and numerical simulations during fluid injection into the smooth and rough faults, respectively. (*B* and *D*) Temporal distributions of induced local slip from numerical modeling during the selected fluid injection stage (the fourth injection stage) for the smooth and rough faults, respectively. Note that the color scale for local slip velocity differs in (*B*) and (*D*). In addition, we map the spatiotemporal distribution of AEs recorded during the corresponding experiment into (*B*) and (*D*), respectively. Because we use a one-dimensional numerical model and assume induced fault slip along fault dip (the major axis of the fault ellipse), we present the experimentally recorded AEs with hypocenters very close to it (radial distance within 5 mm), as indicated by the white solid circles with sizes proportional to AE magnitudes. (*E*) The surface profile of the interface separating the lower and upper blocks for rough fault #1. The gray arrow shows the slip direction of the lower rock block relative to its counterpart along fault up-dip.

negative slopes of surface topography along slip direction, see Fig. 5 *D* and *E*). The low frictional resistances at these fault segments facilitate sliding initiation and impose no major hindrance to slip transfer over the fault surface. Rupture fronts then propagate toward the fault center at a rate of about 0.5 to 1 mm/s. The area with high local stresses in the proximity of the fault center (highly stressed asperities) starts to slip at a later time, but it has a high local slip rate, accompanied by a sharp localized burst in AE activity (Fig. 5*D*). This result agrees with spatial distribution of injection-induced AE activity around high-stress asperities where induced seismic moment release of AEs is high but the associated *b*-value is low (Fig. 3 *E* and *F*). After each fluid injection stage, we find a relatively uniform distribution of cumulative slip across the entire rough fault (*SI Appendix*, Fig. S17).

Discussion

Fault roughness and stress heterogeneity affect earthquake nucleation and propagation and cause complex ruptures, stress drops, slip rate distributions, and off-fault damage zones, as observed in a plethora of studies of tectonic earthquakes and rupture models (8, 16–20). Here, we combine experimental and numerical approaches to demonstrate how fault roughness controls slow stick-slip events induced by fluid injection. In particular, we show that increasing fault roughness stabilizes induced slow stick-slip events. The peak slip velocities of injection-induced slip events and the associated slip-weakening rates are larger for smooth faults, in agreement with earlier friction tests on dry samples (25, 26, 28) and recent numerical modeling results (14, 19).

Following the fault slip-weakening model in the spring-slider system (31), slip acceleration and unstable failure are expected to occur for the fault slip-weakening rate being larger than the stress release rate of the loading system, i.e., the fault stiffness larger than the stiffness of the loading system, otherwise stable slip is expected. The shear stiffness of our loading system (K_{sys}) is about 55 MPa/mm (*SI Appendix*, section 11), resulting in $K_{smooth}/K_{sys} \approx 1.11$ and $K_{rough}/K_{sys} \approx 0.87$ (Fig. 2*E*), respectively. These stiffness ratios are in agreement with the observed macroscopic slow stick-slip on the smooth fault but stable slip on the rough faults. Assuming that the slip patch grows as an expanding crack, the critical nucleation length L_c for slip instability is inversely proportional to the stiffness of the fault patch (31, 69). Nucleation length L_c increasing with fault roughness has been previously reported from laboratory experiments (21, 25, 26, 28) and numerical simulations (12), consistent with our observation.

Friction experiments on dry laboratory faults have shown that roughness significantly influences fault friction constitutive parameters (29–31). In addition to the critical slip-weakening displacement δ_c increasing with fault roughness (25, 26), the characteristic slip displacement d required to change the population of contacts in the rate-and-state friction formulation was also experimentally found to be proportional to surface roughness (31, 32). This agrees with our numerical modeling results that require an increase of d for rough faults to correctly model slip onsets and slip velocities as observed in the experiments. A large δ_c or d is expected to result in larger fracture energies for rough faults (25, 70), limiting acceleration of fault slip during rupture propagation (21). The propagating rupture front is expected to slow down when encountering a region of higher normal stress and shear strength (71), resulting in a lower average slip velocity compared to smooth faults. Once the stored elastic energy is exhausted, the rupture will arrest.

The controlled initial stress levels prior to fluid injection are roughly similar for smooth and rough faults, indicating that stored elastic energy prior to slip is similar for smooth and rough faults. Irrespective of the shear stress level decreasing with slip during fluid injection, induced fault slip and stress drop increase with progressive injection cycles. However, slip velocity and associated AE rates remain similar. This is in contrast to previous injection experiments performed on saw-cut faults in almost impermeable granite samples, where stress drops decrease with progressive fluid injection (48, 51). We attribute the increasing slip and stress drop to changing surface roughness in our sandstone samples with progressive slip and possibly different fault hydraulic properties. AE rates and slip rates are closely correlated for smooth and rough faults.

Our experiments performed on saw-cut and freshly fractured faults with significantly different roughness may represent two end-member fault structures, i.e., mature and immature faults, respectively (1, 5). Similar to previously reported displacement-controlled stick-slip tests (23, 24, 68), our observations suggest that fault roughness affects kinematics of AEs, with an increased fraction of non-double-couple components of AE moment tensors for the rougher faults. Natural earthquakes with non-double-couple mechanisms are commonly attributed to fault complexity (72). For nonplanar faults, the abundant development of intersecting fracture networks and potential damage-related changes of elastic properties in the source region may modify local stress fields and cause the slip vector to deviate from the principal fault surface (7, 24, 59). For the rough faults, we find that injection-induced AE activity localizes in the vicinity of high-stress asperities where substantial seismic moment is released, accompanied by low b-values. The b-value has been suggested to be inversely proportional to stress level (24, 61) and can serve to indicate high stress fault patches (62).

Injection-induced macroscopic fault slip rates in our laboratory experiments remain on the order of micrometers per second, comparable to the reported values of induced fault slip rates measured in a borehole during in situ fluid injection into a natural fault (37). In our experiments, the total seismic moment released by high-frequency AE sources only accounts for a very small part (<0.01%) of total deformation (geodetic) moment release during fluid injection (*SI Appendix*, Fig. S20), consistent with the values reported from in situ fluid injection experiments at different geological settings (37, 73). Such a low ratio indicates that injection-induced fault deformation in our experiments is dominantly aseismic. The estimated source radii of AEs span from 0.1 to 2.6 mm (*SI Appendix*, section 7), far smaller than the macroscopic fault size. In this sense, our laboratory AE sources associated with induced fault slip may be more representative of injection-induced confined ruptures occurring within limited zones of distributed fractures in nature. To further link our laboratory observations to fluid-induced seismicity in the field, we have compiled a wide range of datasets of radiated seismic energy as a function of hydraulic energy from laboratory-scale and in situ fluid injection experiments, as well as reservoir-scale fracturing, geothermal and disposal projects across the world (Fig. 6). The ratio of seismic energy to hydraulic energy is termed seismic injection efficiency (74). The seismic injection efficiencies in our experiments range between 10^{-7} and 10^{-6}, in agreement with the reported laboratory hydraulic fracturing experiments (75), in situ fluid injection experiments (73, 76) and some field-scale induced earthquakes (74, 77). The values of seismic injection efficiency for field-scale earthquakes associated with fluid injection vary over nine orders of magnitude from 10^{-9} to 1, and even above 1. For example, the large seismic injection efficiency up to 1.8 for the M_W 5.5 Pohang earthquake indicates that more energy was radiated seismically than hydraulically injected, suggesting a runaway rupture beyond the region perturbed by injection (42, 77). These large seismic events with high seismic injection efficiency $>10^{-3}$ are attributed to substantial release of tectonic strain energy by activation of runaway ruptures, where rupture size may be only limited by the size of tectonic faults (41, 42, 74, 77). In contrast, induced seismicity showing an extended pressure-controlled rupture in a self-arrested manner typically shows a low seismic injection efficiency $<10^{-3}$ (74, 75, 77). Thus, our laboratory observations bear similarities with those field-scale induced earthquakes corresponding to pressure-controlled ruptures, as reflected by the fact that in our experiments the induced fault slip terminates shortly after we stop fluid injection (Fig. 2).

To summarize our experimental observations and modeling results, we propose a conceptual model of injection-induced fault reactivation (Fig. 7). We assume uniform fault friction in space but an initially heterogeneous distribution of normal and shear stresses depending on fault surface topography (Fig. 7*A*). With increasing fluid pressure slow aseismic creep, possibly with few seismic events, will commence at favorably oriented and weak fault segments once local strength is exceeded (Fig. 7*B*). As fluid pressure progressively increases, the creeping patches are expected to expand and load

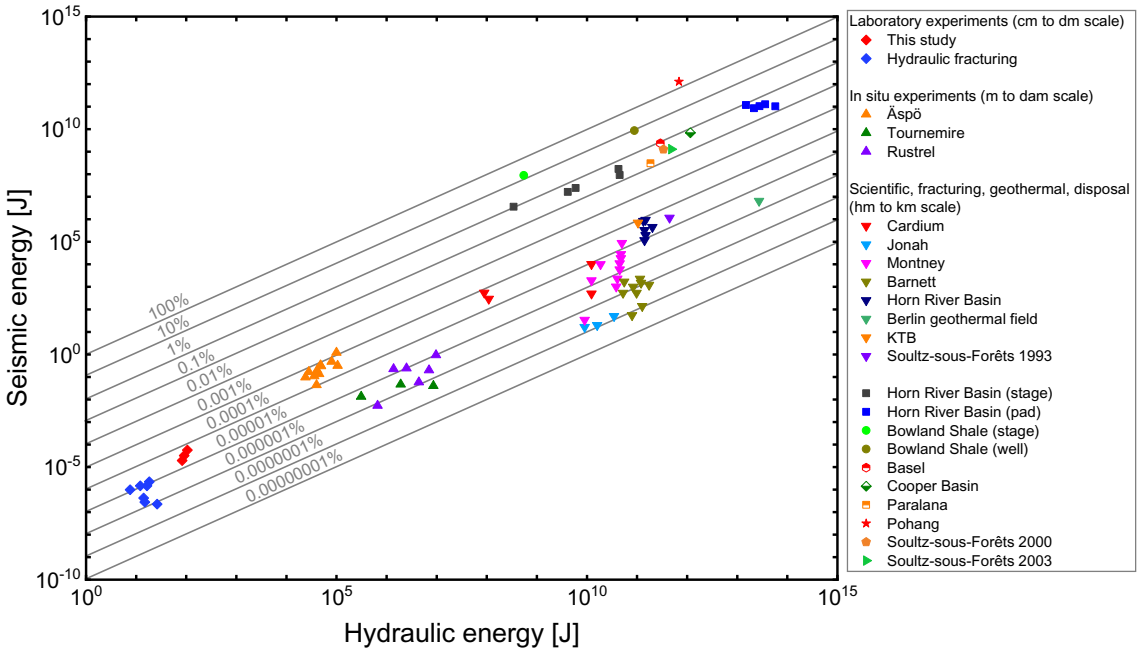

Fig. 6. The relation between cumulative seismic energy and cumulative hydraulic energy across a wide range of length scales. For the laboratory experiments, the seismic energy is determined from the radiated AEs in the present study and in the hydraulic fracturing experiments by Goodfellow et al. (75). In situ fluid injection experiments performed at the Underground Laboratory of Tournemire (France) and at the Underground Laboratory of Rustrel (France) are from ref. 73, while the in situ hydraulic fracturing experiments performed at the Underground Äspö Hard Rock Laboratory (Sweden) are from ref. 76. The datasets for reservoir-scale seismicity associated with fluid injection are compiled from refs. 74, 75, and 77. Reference gray lines correspond to the seismic injection efficiency (the ratio of seismic energy to hydraulic energy) in percentages.

high-strength asperities nearby. Fluid-induced aseismic creep leading to seismic slip has been described also for in situ injection experiments (37) and reservoir-scale hydraulic fracturing-induced seismicity (78). Once the failure strength of the asperities is exceeded, clustered and increasing seismic activity containing progressively larger events will occur (Fig. 7*C*). This may initiate large events, produce high local stress drops and slip rates, large seismic moment release and low *b*-values, as observed in our experiments. Previous studies have revealed the important effects of heterogeneous fault frictional properties (36) and the interplay between permeability change and ongoing fault slip (37, 52) during fluid injection, which are expected to be minimized in our experiments due to the usage

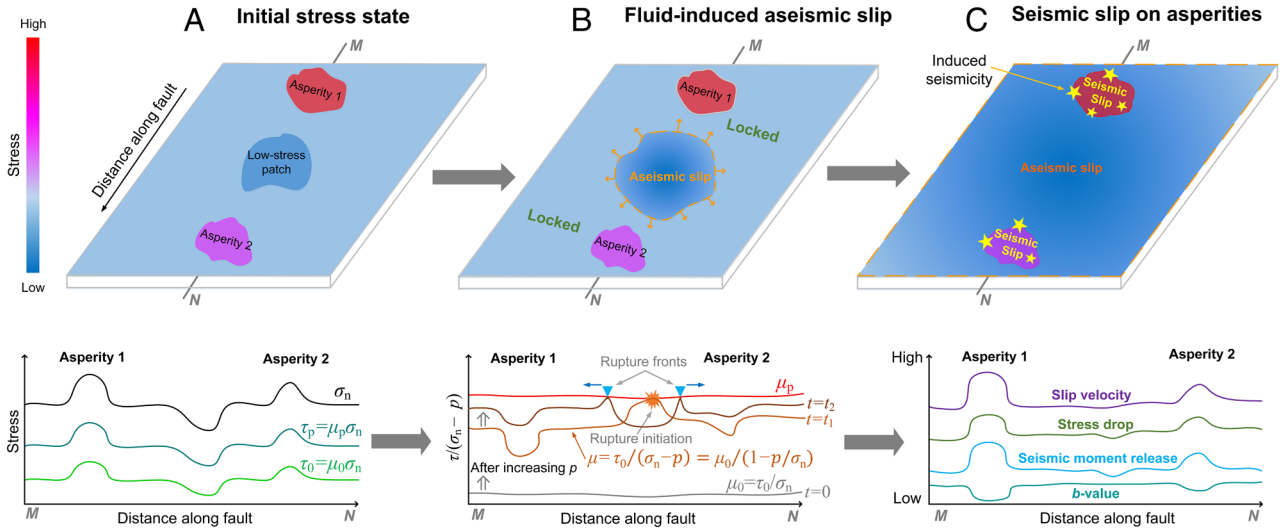

Fig. 7. Schematic illustration of fluid-induced seismicity on a spatially heterogeneous fault with permeable structures. (*A*) Prior to fluid overpressure, the initial state of a heterogeneous fault shows a spatial variation in initial stress and strength. We assume relatively uniform initial and peak friction coefficients (denoted by μ_0 and μ_p, respectively) in space, but initial normal stress σ_n shows a significantly heterogeneous distribution. This scenario results in spatially heterogeneous shear stress τ_0 and shear strength τ_p before fluid pressure perturbations. Here, asperities are defined as local patches with high initial stress and strength. (*B*) After a relatively homogeneous fluid overpressure p is imposed, the apparent friction coefficient $\tau/(\sigma_n-p)$ of fault segments starts to increase at different rates, depending on the initial normal stress distribution. Injection-induced aseismic slip first occurs on the weak patches with low local strength, and then, the slow creeping zone continues to expand with progressive fluid pressurization and increases shear stress at propagating creep fronts. (*C*) Large failure events and seismic slip ultimately take place around the asperities due to stress transfer from aseismic slip. Induced seismicity is expected to occur around these highly stressed patches, accompanied by high local stress drops and slip rates, large seismic moment release, and low Gutenberg–Richter *b*-values. The figures in the bottom row correspond to one-dimensional profiles along fault distance at different stages.

of rock materials being isotropic, homogeneous, and permeable. We highlight that fault roughness may modulate the aseismic-seismic slip transition for permeable fault structures subjected to increased fluid pressures. The reservoir structures dominated by rough and segmented faults and fractures are expected to host nucleation processes that happen at larger length and time scales during fluid injection, possibly captured by geodetic and broad-band seismological instruments. Our findings imply that when monitoring fluid injections in geological reservoirs is done in real time (41), this may allow identifying localization processes of induced microseismicity prior to future larger induced events. Feeding this information into the next-generation traffic-light systems might allow providing additional constraints for stopping injection before larger induced seismic events occur around the highly stressed fault patches.

Materials and Methods

Experimental Setup. We conducted fluid injection experiments on three cylindrical samples of homogeneous, isotropic, and permeable Bentheim sandstone at crustal pressure conditions using a servo-hydraulic MTS apparatus (stiffness of ~0.65×10^9 N/m) equipped with an AE recording system and a pore pressure system (two Quizix 6000 pumps at downstream and upstream, respectively). One sample contained a saw-cut (smooth) fault, and two samples were cut by fractured rough faults (hereafter named rough fault #1 and rough fault #2, respectively). The rms height (h_{rms}) of saw-cut fault surface was measured to be about 0.044 mm, whereas the values of h_{rms} were increased to about 1.50 mm and 0.82 mm for rough fault #1 and rough fault #2, respectively (*SI Appendix*, section 1). The three faults were all oriented at $\phi = 30°$ to the cylinder axis (Fig. 1*A*). To measure deformation and record seismic activity, eight local strain gauges and 16 piezoelectric transducers (PZTs) were mounted to the sample surface before experiments (*SI Appendix*, sections 2 and 3 and Fig. S1). The samples were first hydrostatically loaded up to 35 MPa ($\sigma_3 = 35$ MPa) while the fluid pressure (p) was kept constant at 5 MPa. Next, we increased the axial stress (σ_1) at a constant axial displacement rate of 1 μm/s to achieve the peak shear strength (τ_{ss}) resolved on the fault interface. We then reduced axial stress slowly until the calculated shear stress (τ) along the fault interface equaled about 0.92 τ_{ss} for the smooth fault and rough fault #1 and 0.86 τ_{ss} for rough fault #2, respectively. This guaranteed that the laboratory faults were near the critical stress state before fluid injection. Note that because of the sample geometry, increasing the axial stress results in an increase in both shear and normal stresses. The position of the axial hydraulic cylinder was then kept constant, and eventually, we injected distilled water into the samples from the bottom end to induce fault slip at undrained conditions. The fluid pressure was increased in a stepwise manner from 5 MPa to 29 MPa with a pressurization rate of 2 MPa/min. We divided the whole fluid injection process into six stages, and each stage had a duration of 10 min composed of a ramp phase lasting for 2 min (to fulfill 4 MPa fluid increment) and a subsequent plateau phase for 8 min.

Processing of Hydraulic, Mechanical, and Acoustic Emission Data. The details of stress and slip measurements are given in *SI Appendix*, section 4. The details of acoustic emission (AE) data processing including the spatial distribution, frequency–magnitude characteristics, and source mechanisms are provided in *SI Appendix*, sections 5–8. The calculation details of hydraulic energy and seismic energy are available in *SI Appendix*, section 9.

Numerical Model. To reproduce the observed injection-induced fault slip on the smooth and rough faults, we extend the one-dimensional (1D) Burridge–Knopoff model (79) for heterogeneously loaded interfaces obeying the rate-and-state friction law by encompassing the fluid pressure diffusion process.

The 1D Burridge–Knopoff model consists of an array of N identical blocks that are interconnected by elastic springs with stiffness coefficient λ and are elastically driven (with spring stiffness coefficient k) by a rigid plate moving at a constant velocity v_{lp} (analogous to far-field tectonic motions) (*SI Appendix*, Fig. S14). This model has been previously used to investigate frictional slip along a rough surface (79). To simulate effects of fluid pressure, we account for a local fluid pressure distribution acting on the chain of blocks in addition to varying normal stresses. For each block, the frictional slip is governed by an empirical rate-and-state friction law (31, 32), that is, its friction coefficient μ_i varies with the instantaneous slip rate v_i and the state variable θ_i (the subscript i means the block index), as expressed by:

$$\mu_i = \mu^* + a_i \ln\left(v_i / v^*\right) + b_i \ln\left(v^* \theta_i / d_i\right), \quad [1]$$

where μ^* indicates the reference friction coefficient at a steady-state reference sliding velocity v^*, and d_i represents the characteristic slip distance over which friction evolves to a new steady state after a velocity perturbation, a and b are frictional parameters that describe the friction response to a sudden step jump of the imposed velocity for a single spring-block configuration. The sign of $(a-b)$ defines the change of the steady-state friction coefficient with velocity in which $a > b$ means velocity-strengthening and velocity-weakening corresponds to $a < b$. We constrain the evolution of state variable θ_i with time t using the slip law because it provides a better match to laboratory data (80), as given by:

$$\frac{d\theta_i}{dt} = -\frac{v^* \theta_i}{d_i} \ln\left(\frac{v^* \theta_i}{d_i}\right). \quad [2]$$

To mimic our experimental configuration, we assume that fluid overpressure is imposed at a remote injection port with a given time-varying injection pressure p_∞. Fluid pressure diffusion through rock matrix with hydraulic diffusivity c toward the fault zone modifies the effective stress states for fault segments and thus may cause fault reactivation.

Assuming the membrane diffusion process (fluid pressure evolution within the fault zone depends linearly on the fluid pressure difference between the fault zone and the remote fluid pressure) that is typically suitable for laboratory experiment scenarios (81), evolving fluid pressure within the fault zone can be constrained by:

$$c_i^* \left(p_\infty - p_i\right) = \frac{\partial p_i}{\partial t}, \quad [3]$$

where p_i indicates the fluid pressure acting on the ith block within the fault zone, p_∞ refers to the pore pressure at the remote injection port, and c_i^* is given by $c_i^* = c/L_i^2$ with L_i being a characteristic diffusion length between the remote injection port and the ith block and c being the hydraulic diffusivity. Considering the high permeability of the rock matrix adopted in our experiments, the effect of shear-induced dilation/compaction on the modification of fluid pressure within the fault zone and on fault slip can be negligible.

For a chain of spring-connected blocks driven by a moving plate and subjected to normal stress and fluid pressure, the equation of motion for the ith block's position x_i in the quasi-dynamic sense (i.e., the inertial effect is replaced by a radiation damping term) is given by Rice (69)

$$\left(\sigma_{n,i} - p_i\right)\mu_i = k\left(v_{lp} t - x_i\right) + \lambda\left(x_{i+1} - 2x_i + x_{i-1}\right) - \eta v_i, \quad [4]$$

where $\sigma_{n,i}$ and p_i are the normal stress and fluid pressure applied to the ith block, k is the spring constant connecting each block to a moving plate with a constant velocity v_{lp}, λ is the spring stiffness coupling the neighboring blocks, x_i is the position of the ith block with respect to its initial starting position, v_i is the slip velocity of ith block ($v_i = dx_i/dt$), and η describes radiation damping, constrained by $\eta = G/2V_s$ in which G is the shear modulus of the rock and V_s is shear wave velocity (69). For a given number of blocks subjected to heterogeneous normal stress distributions, combining Eqs. **1**–**4** and solving them jointly with the Runge–Kutta method can simulate the injection-induced fault slip on a rough surface in response to a given injection pressure perturbation.

We use the equally spaced 100 blocks with a grid spacing of 1 mm (i.e., the block size) to capture the behavior of the 100-mm-long laboratory faults along the dip direction. The input parameters are given in *SI Appendix*, section 11 and Table S1.

Data, Materials, and Software Availability. The experimental data are archived in Mendeley Data accessible at https://data.mendeley.com/datasets/xcyvspjk3c/1 (DOI: 10.17632/xcyvspjk3c.1) (82). All other data are included in the article and/or supporting information.

ACKNOWLEDGMENTS. We thank Stefan Gehrmann for assistance with sample preparation and thin sections. We are grateful to Valerian Schuster for thin-section microscopy observations. The manuscript benefited from the constructive discussions with Jay Fineberg, Thomas Goebel, and Nicolas Brantut. We thank two reviewers Paul Segall and Greg Hirth, and the Editor for insightful comments and suggestions that have greatly improved the present study. L.W. acknowledges in-house postdoc funding provided by Helmholtz Centre Potsdam, GFZ German Research Centre for Geosciences. G.D. acknowledges funding from BMBF project STIMTEC–X 03G0901C.

Author affiliations: [a]Helmholtz Centre Potsdam, GFZ German Research Centre for Geosciences, Geomechanics and Scientific Drilling, Potsdam 14473, Germany; [b]The Njord Centre, Department of Geosciences, University of Oslo, Oslo 0316, Norway; [c]The Njord Centre, Department of Physics, University of Oslo, Oslo 0316, Norway; [d]ISTerre, Université Grenoble Alpes, Grenoble INP, Université Savoie Mont Blanc, CNRS, IRD, Université Gustave Eiffel, Grenoble 38000, France; [e]Laboratory of Experimental Rock Mechanics, Civil Engineering Institute, École Polytechnique Fédérale de Lausanne, Lausanne 1015, Switzerland; [f]Department of Earth Sciences, Free University Berlin, Berlin 12249, Germany; and [g]Institute of Earth and Environmental Science, University of Potsdam, Potsdam 14469, Germany

1. A. Sagy, E. E. Brodsky, G. J. Axen, Evolution of fault-surface roughness with slip. *Geology* **35**, 283–286 (2007).
2. W. L. Power, T. E. Tullis, Euclidean and fractal models for the description of rock surface roughness. *J. Geophys. Res. Solid Earth* **96**, 415–424 (1991).
3. E. E. Brodsky, J. D. Kirkpatrick, T. Candela, Constraints from fault roughness on the scale-dependent strength of rocks. *Geology* **44**, 19–22 (2016).
4. F. Renard, T. Candela, E. Bouchaud, Constant dimensionality of fault roughness from the scale of micro-fractures to the scale of continents. *Geophys. Res. Lett.* **40**, 83–87 (2013).
5. T. Candela *et al.*, Roughness of fault surfaces over nine decades of length scales. *J. Geophys. Res. Solid Earth* **117**, B08409 (2012).
6. J. H. Dieterich, B. D. Kilgore, Direct observation of frictional contacts: New insights for state-dependent properties. *Pure Appl. Geophys.* **143**, 283–302 (1994).
7. F. M. Chester, J. S. Chester, Stress and deformation along wavy frictional faults. *J. Geophys. Res. Solid Earth* **105**, 23421–23430 (2000).
8. J. H. Dieterich, D. E. Smith, Nonplanar faults: Mechanics of slip and off-fault damage. *Pure Appl. Geophys.* **166**, 1799–1815 (2009).
9. S. R. Brown, C. H. Scholz, Closure of random elastic surfaces in contact. *J. Geophys. Res. Solid Earth* **90**, 5531–5545 (1985).
10. Z. Fang, E. M. Dunham, Additional shear resistance from fault roughness and stress levels on geometrically complex faults. *J. Geophys. Res. Solid Earth* **118**, 3642–3654 (2013).
11. N. Yoshioka, C. H. Scholz, Elastic properties of contacting surfaces under normal and shear loads: 1. Theory. *J. Geophys. Res. Solid Earth* **94**, 17681–17690 (1989).
12. Y. Tal, B. H. Hager, J. P. Ampuero, The effects of fault roughness on the earthquake nucleation process. *J. Geophys. Res. Solid Earth* **123**, 437–456 (2018).
13. S. W. Ozawa, T. Hatano, N. Kame, Longer migration and spontaneous decay of aseismic slip pulse caused by fault roughness. *Geophys. Res. Lett.* **46**, 636–643 (2019).
14. C. Cattania, P. Segall, Precursory slow slip and foreshocks on rough faults. *J. Geophys. Res. Solid Earth* **126**, e2020JB020430 (2021).
15. S. Ozawa, R. Ando, Mainshock and aftershock sequence simulation in geometrically complex fault zones. *J. Geophys. Res. Solid Earth* **126**, e2020JB020865 (2021).
16. A. A. Allam, K. A. Kroll, C. W. D. Milliner, K. B. Richards-Dinger, Effects of fault roughness on coseismic slip and earthquake locations. *J. Geophys. Res. Solid Earth* **124**, 11336–11349 (2019).
17. Z. Shi, S. M. Day, Rupture dynamics and ground motion from 3-D rough-fault simulations. *J. Geophys. Res. Solid Earth* **118**, 1122–1141 (2013).
18. O. Zielke, M. Galis, P. M. Mai, Fault roughness and strength heterogeneity control earthquake size and stress drop. *Geophys. Res. Lett.* **44**, 777–783 (2017).
19. Y. Tal, B. H. Hager, The slip behavior and source parameters for spontaneous slip events on rough faults subjected to slow tectonic loading. *J. Geophys. Res. Solid Earth* **123**, 1810–1823 (2018).
20. E. M. Dunham, D. Belanger, L. Cong, J. E. Kozdon, Earthquake ruptures with strongly rate-weakening friction and off-fault plasticity, part 2: Nonplanar faults. *Bull. Seismol. Soc. Am.* **101**, 2308–2322 (2011).
21. A. Gounon, S. Latour, J. Letort, S. El Arem, Rupture nucleation on a periodically heterogeneous interface. *Geophys. Res. Lett.* **49**, e2021GL096816 (2022).
22. F. Yamashita *et al.*, Rupture preparation process controlled by surface roughness on meter-scale laboratory fault. *Tectonophysics* **733**, 193–208 (2018).
23. G. Dresen, G. Kwiatek, T. Goebel, Y. Ben-Zion, Seismic and aseismic preparatory processes before large stick-slip failure. *Pure Appl. Geophys.* **177**, 5741–5760 (2020).
24. T. H. W. Goebel, G. Kwiatek, T. W. Becker, E. E. Brodsky, G. Dresen, What allows seismic events to grow big?: Insights from b-value and fault roughness analysis in laboratory stick-slip experiments. *Geology* **45**, 815–818 (2017).
25. P. G. Okubo, J. H. Dieterich, Effects of physical fault properties on frictional instabilities produced on simulated faults. *J. Geophys. Res. Solid Earth* **89**, 5817–5827 (1984).
26. M. Ohnaka, L. Shen, Scaling of the shear rupture process from nucleation to dynamic propagation: Implications of geometric irregularity of the rupturing surfaces. *J. Geophys. Res. Solid Earth* **104**, 817–844 (1999).
27. S. Guérin-Marthe *et al.*, Preparatory slip in laboratory faults: Effects of roughness and load point velocity. *J. Geophys. Res. Solid Earth* **128**, e2022JB025511 (2023).
28. S. Xu *et al.*, Fault strength and rupture process controlled by fault surface topography. *Nat. Geosci.* **16**, 94–100 (2023).
29. C. W. A. Harbord, S. B. Nielsen, N. De Paola, R. E. Holdsworth, Earthquake nucleation on rough faults. *Geology* **45**, 931–934 (2017).
30. A. M. Eijsink, J. D. Kirkpatrick, F. Renard, M. J. Ikari, Fault surface morphology as an indicator for earthquake nucleation potential. *Geology* **50**, 1356–1360 (2022).
31. J. H. Dieterich, Modeling of rock friction: 1. Experimental results and constitutive equations. *J. Geophys. Res. Solid Earth* **84**, 2161–2168 (1979).
32. C. Marone, Laboratory-derived friction laws and their application to seismic faulting. *Annu. Rev. Earth Planet. Sci.* **26**, 643–696 (1998).
33. F. Yamashita *et al.*, Two end-member earthquake preparations illuminated by foreshock activity on a meter-scale laboratory fault. *Nat. Commun.* **12**, 1–11 (2021).
34. W. L. Ellsworth, Injection-induced earthquakes. *Science (80-)* **341**, 1225942 (2013).
35. R. Schultz *et al.*, Hydraulic fracturing-induced seismicity. *Rev. Geophys.* **58**, e2019RG000695 (2020).
36. F. Cappa, M. M. Scuderi, C. Collettini, Y. Guglielmi, J.-P. Avouac, Stabilization of fault slip by fluid injection in the laboratory and in situ. *Sci. Adv.* **5**, eaau4065 (2019).
37. Y. Guglielmi, F. Cappa, J.-P. Avouac, P. Henry, D. Elsworth, Seismicity triggered by fluid injection–induced aseismic slip. *Science (80-)* **348**, 1224–1226 (2015).
38. M. Weingarten, S. Ge, J. W. Godt, B. A. Bekins, J. L. Rubinstein, High-rate injection is associated with the increase in U.S. mid-continent seismicity. *Science (80-)* **348**, 1336–1340 (2015).
39. C. Langenbruch, M. D. Zoback, How will induced seismicity in Oklahoma respond to decreased saltwater injection rates? *Sci. Adv.* **2**, e1601542 (2016).
40. J. H. Healy, W. W. Rubey, D. T. Griggs, C. B. Raleigh, The denver earthquakes. *Science (80-)* **161**, 1301–1310 (1968).
41. G. Kwiatek *et al.*, Controlling fluid-induced seismicity during a 6.1-km-deep geothermal stimulation in Finland. *Sci. Adv.* **5**, eaav7224 (2019).
42. M. Galis, J. P. Ampuero, P. M. Mai, F. Cappa, Induced seismicity provides insight into why earthquake ruptures stop. *Sci. Adv.* **3**, eaap7528 (2017).
43. A. McGarr, Maximum magnitude earthquakes induced by fluid injection. *J. Geophys. Res. Solid Earth* **119**, 1008–1019 (2014).
44. S. A. Shapiro, O. S. Krüger, C. Dinske, C. Langenbruch, Magnitudes of induced earthquakes and geometric scales of fluid-stimulated rock volumes. *Geophysics* **76**, WC55–WC63 (2011).
45. L. Wang *et al.*, Laboratory study on fluid-induced fault slip behavior: The role of fluid pressurization rate. *Geophys. Res. Lett.* **47**, e2019GL086627 (2020).
46. L. Wang, G. Kwiatek, E. Rybacki, M. Bohnhoff, G. Dresen, Injection-induced seismic moment release and laboratory fault slip: Implications for fluid-induced seismicity. *Geophys. Res. Lett.* **47**, e2020GL089576 (2020).
47. F. X. Passelègue, N. Brantut, T. M. Mitchell, Fault reactivation by fluid injection: Controls from stress state and injection rate. *Geophys. Res. Lett.* **45**, 12837–12846 (2018).
48. Y. Ji, L. Wang, H. Hofmann, G. Kwiatek, G. Dresen, High-rate fluid injection reduces the nucleation length of laboratory earthquakes on critically stressed faults in granite. *Geophys. Res. Lett.* **49**, e2022GL100418 (2022).
49. D. I. Garagash, L. N. Germanovich, Nucleation and arrest of dynamic slip on a pressurized fault. *J. Geophys. Res. Solid Earth* **117**, B10310 (2012).
50. S. B. L. Cebry, C. Y. Ke, G. C. McLaskey, The role of background stress state in fluid-induced aseismic slip and dynamic rupture on a 3-m laboratory fault. *J. Geophys. Res. Solid Earth* **127**, e2022JB024371 (2022).
51. F. X. Passelègue *et al.*, Initial effective stress controls the nature of earthquakes. *Nat. Commun.* **11**, 5132 (2020).
52. F. Cappa, Y. Guglielmi, C. Nussbaum, L. De Barros, J. Birkholzer, Fluid migration in low-permeability faults driven by decoupling of fault slip and opening. *Nat. Geosci.* **15**, 747–751 (2022).
53. K. A. Kroll, E. S. Cochran, Stress controls rupture extent and maximum magnitude of induced earthquakes. *Geophys. Res. Lett.* **48**, e2020GL092148 (2021).
54. J. Maurer, E. M. Dunham, P. Segall, Role of fluid injection on earthquake size in dynamic rupture simulations on rough faults. *Geophys. Res. Lett.* **47**, e2020GL088377 (2020).
55. Z. Ye, A. Ghassemi, Injection-induced shear slip and permeability enhancement in granite fractures. *J. Geophys. Res. Solid Earth* **123**, 9009–9032 (2018).
56. Y. Ji, W. Wu, Injection-driven fracture instability in granite: Mechanism and implications. *Tectonophysics* **791**, 228572 (2020).
57. B. Kc, E. Ghazanfari, Geothermal reservoir stimulation through hydro-shearing: An experimental study under conditions close to enhanced geothermal systems. *Geothermics* **96**, 102200 (2021).
58. L. Wang, E. Rybacki, A. Bonnelye, M. Bohnhoff, G. Dresen, Experimental investigation on static and dynamic bulk moduli of dry and fluid-saturated porous sandstones. *Rock Mech. Rock Eng.* **54**, 129–148 (2021).
59. P. Segall, D. D. Pollard, Mechanics of discontinuous faults. *J. Geophys. Res. Solid Earth* **85**, 4337–4350 (1980).
60. R. H. Sibson, Stopping of earthquake ruptures at dilational fault jogs. *Nature* **316**, 248–251 (1985).
61. C. H. Scholz, On the stress dependence of the earthquake b value. *Geophys. Res. Lett.* **42**, 1399–1402 (2015).
62. S. Wiemer, M. Wyss, Mapping the frequency-magnitude distribution in asperities: An improved technique to calculate recurrence times? *J. Geophys. Res. Solid Earth* **102**, 15115–15128 (1997).
63. P. M. Powers, T. H. Jordan, Distribution of seismicity across strike-slip faults in California. *J. Geophys. Res. Solid Earth* **115**, 5305 (2010).
64. A. Zang *et al.*, Source analysis of acoustic emissions in Aue granite cores under symmetric and asymmetric compressive loads. *Geophys. J. Int.* **135**, 1113–1130 (1998).
65. G. Kwiatek, P. Martínez-Garzón, M. Bohnhoff, HybridMT: A MATLAB/Shell environment package for seismic moment tensor inversion and refinement. *Seismol. Res. Lett.* **87**, 964–976 (2016).
66. J. A. Hudson, R. G. Pearce, R. M. Rogers, Source type plot for inversion of the moment tensor. *J. Geophys. Res. Solid Earth* **94**, 765–774 (1989).
67. J. Davidsen *et al.*, What controls the presence and characteristics of aftershocks in rock fracture in the lab? *J. Geophys. Res. Solid Earth* **126**, e2021JB022539 (2021).
68. G. Kwiatek, T. H. W. Goebel, G. Dresen, Seismic moment tensor and b value variations over successive seismic cycles in laboratory stick-slip experiments. *Geophys. Res. Lett.* **41**, 5838–5846 (2014).
69. J. R. Rice, Spatio-temporal complexity of slip on a fault. *J. Geophys. Res. Solid Earth* **98**, 9885–9907 (1993).
70. A. M. Rubin, J.-P. Ampuero, Earthquake nucleation on (aging) rate and state faults. *J. Geophys. Res. Solid Earth* **110**, B11312 (2005).

71. K. Aki, Characterization of barriers on an earthquake fault. *J. Geophys. Res. Solid Earth* **84**, 6140–6148 (1979).
72. C. Frohlich, Earthquakes with non-double-couple mechanisms. *Science* **264**, 804–809 (1994).
73. L. De Barros, F. Cappa, Y. Guglielmi, L. Duboeuf, J. R. Grasso, Energy of injection-induced seismicity predicted from in-situ experiments. *Sci. Rep.* **9**, 4999 (2019).
74. S. Maxwell, Unintentional seismicity induced by hydraulic fracturing. *CSEG Rec.* **38**, 40–49 (2013).
75. S. D. Goodfellow, M. H. B. Nasseri, S. C. Maxwell, R. P. Young, Hydraulic fracture energy budget: Insights from the laboratory. *Geophys. Res. Lett.* **42**, 3179–3187 (2015).
76. G. Kwiatek *et al.*, Insights into complex subdecimeter fracturing processes occurring during a water injection experiment at depth in äspö hard rock laboratory, Sweden. *J. Geophys. Res. Solid Earth* **123**, 6616–6635 (2018).
77. S. Bentz, G. Kwiatek, P. Martínez-Garzón, M. Bohnhoff, G. Dresen, Seismic moment evolution during hydraulic stimulations. *Geophys. Res. Lett.* **47**, e2019GL086185 (2020).
78. T. S. Eyre *et al.*, The role of aseismic slip in hydraulic fracturing–induced seismicity. *Sci. Adv.* **5**, eaav7172 (2019).
79. R. Burridge, L. Knopoff, Model and theoretical seismicity. *Bull. Seismol. Soc. Am.* **57**, 341–371 (1967).
80. P. Bhattacharya, A. M. Rubin, E. Bayart, H. M. Savage, C. Marone, Critical evaluation of state evolution laws in rate and state friction: Fitting large velocity steps in simulated fault gouge with time-, slip-, and stress-dependent constitutive laws. *J. Geophys. Res. Solid Earth* **120**, 6365–6385 (2015).
81. P. Segall, J. R. Rice, Dilatancy, compaction, and slip instability of a fluid-infiltrated fault. *J. Geophys. Res. Solid Earth* **100**, 22155–22171 (1995).
82. L. Wang, Supplementary Data for the study of 'Fault roughness controls injection-induced seismicity'. Mendeley Data, V1. https://data.mendeley.com/datasets/xcyvspjk3c/1. Deposited 22 May 2023.